

A Two-Step Absorber Deposition Approach To Overcome Shunt Losses in Thin-Film Solar Cells: Using Tin Sulfide as a Proof-of-Concept Material System

Vera Steinmann,^{*,†} Rupak Chakraborty,[†] Paul H. Rekemeyer,[‡] Katy Hartman,[†] Riley E. Brandt,[†] Alex Polizzotti,[†] Chuanxi Yang,[§] Tom Moriarty,^{||} Silviya Gradečak,[‡] Roy G. Gordon,[§] and Tonio Buonassisi^{*,†}

[†]Department of Mechanical Engineering, Massachusetts Institute of Technology, Cambridge, Massachusetts 02139, United States

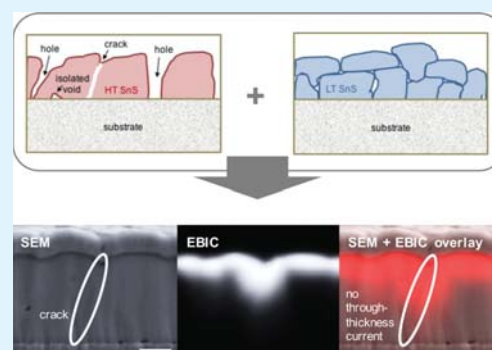
[‡]Department of Materials Science and Engineering, Massachusetts Institute of Technology, Cambridge, Massachusetts 02139, United States

[§]Department of Chemistry and Chemical Biology, Harvard University, Cambridge, Massachusetts 02138 United States

^{||}National Renewable Energy Laboratory, Golden, Colorado 80401, United States

ABSTRACT: As novel absorber materials are developed and screened for their photovoltaic (PV) properties, the challenge remains to reproducibly test promising candidates for high-performing PV devices. Many early-stage devices are prone to device shunting due to pinholes in the absorber layer, producing “false-negative” results. Here, we demonstrate a device engineering solution toward a robust device architecture, using a two-step absorber deposition approach. We use tin sulfide (SnS) as a test absorber material. The SnS bulk is processed at high temperature (400 °C) to stimulate grain growth, followed by a much thinner, low-temperature (200 °C) absorber overlayer. At a lower process temperature, the thin absorber overlayer contains significantly smaller, densely packed grains, which are likely to provide a continuous coating and fill pinholes in the underlying absorber bulk. We compare this two-step approach to the more standard approach of using a semi-insulating buffer layer directly on top of the annealed absorber bulk, and we demonstrate a more than 3.5× superior shunt resistance R_{sh} with smaller standard error $\sigma_{R_{sh}}$. Electron-beam-induced current (EBIC) measurements indicate a lower density of pinholes in the SnS absorber bulk when using the two-step absorber deposition approach. We correlate these findings to improvements in the device performance and device performance reproducibility.

KEYWORDS: thin-films, photovoltaics, novel absorber materials, tin sulfide, device shunting, performance reliability



1. INTRODUCTION

The rapid performance improvement of lead halide perovskite solar cells has spurred the search for nontoxic, earth-abundant perovskite-inspired photovoltaic (PV) materials.^{1–3} To validate the PV potential of these candidates, it remains an important challenge to demonstrate high-performing PV devices. Many early-stage devices based on new-emerging perovskite-inspired absorber materials are prone to device shunting due to pinholes in the absorber layer, caused by unoptimized fabrication processes.^{4–6} There is the danger that early-stage low-power conversion efficiencies (PCE) due to shunting effects may contribute to “false negative” results. Hence, there is an urgent need to engineer more robust device architectures that allow for rapid PV device performance testing of novel absorbers without sacrificing device performance due to shunting losses. Yokoyama et al. have recently introduced a modified vapor-assisted solution-processing method for more uniform and pinhole-free thin-film fabrication via solution.⁷ Pinhole treat-

ments in thin-films has previously been developed for large area amorphous silicon⁸ as well as cadmium telluride solar cells.⁹

Tin sulfide is a promising, emerging thin-film absorber candidate; tin (Sn) and sulfur (S) are both scalable and nontoxic constituents. The SnS molecule congruently evaporates as one molecule at temperatures below 600 °C, allowing for potentially low manufacturing costs. Due to its high optical absorption coefficient in the visible spectrum ($>10^5 \text{ cm}^{-1}$),^{10–12} film thicknesses below 1 μm are sufficient to absorb most of the incident sunlight. Despite its promising PV properties, devices based on SnS are still underperforming compared to the theoretical maximum efficiency of 32%, assuming a bandgap of 1.1 eV.¹³ In recent years NREL certified record efficiencies of $\eta = 3.88\%$ and $\eta = 4.36\%$ have been achieved via thermal

Received: June 14, 2016

Accepted: August 5, 2016

evaporation (TE) and atomic layer deposition (ALD), respectively.^{14,15}

A performance loss analysis of TE SnS solar cells suggests that the device performance and performance reproducibility of TE SnS solar cells is affected by a low shunt resistance R_{sh} ($74 \Omega \text{ cm}^2$), which reduces the fill factor (FF) and open-circuit voltage V_{OC} .¹⁴ The low shunt resistance might result from pinholes in the SnS bulk and current pathways around the edges of the device.¹⁴ Experimental data of identically fabricated one-step deposition baseline devices indeed reveals a correlation between the shunt resistance and the V_{OC} , as shown in Figure 1. A low $R_{sh} < 200 \Omega \text{ cm}^2$ limits the V_{OC}

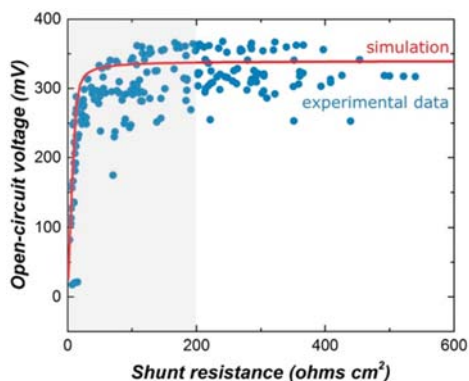


Figure 1. Open-circuit voltage V_{OC} of identically fabricated SnS one-step deposition baseline devices plotted as a function of the illuminated shunt resistance R_{sh} . An increase in R_{sh} leads to an increase in V_{OC} and a smaller standard error in V_{OC} . The trend in experimental data (blue dots) matches the expected trend seen in device simulations (red line), when varying the R_{sh} , using a previously developed optoelectronic model¹⁶ with all other device parameters kept constant at the values used in reference.¹⁶ The gray shaded area highlights the regime of low R_{sh} resulting in low V_{OC} . For $R_{sh} > 200 \Omega \text{ cm}^2$, the number of devices with a V_{OC} of $(330 \pm 30) \text{ mV}$ significantly increases with the exception of only three outliers showing a V_{OC} well below 300 mV.

potential and reproducibility of the device (see gray-shaded area). For $R_{sh} > 200 \Omega \text{ cm}^2$, the number of devices with a V_{OC} of $(330 \pm 30) \text{ mV}$ significantly increases. Figure 1 reveals only three outliers with a V_{OC} well below 300 mV for $R_{sh} > 200 \Omega \text{ cm}^2$. Overall, a higher shunt resistance enables a higher V_{OC} and improves performance reproducibility. The trend in experimental data (blue dots) matches the expected trend seen in device simulations (red line), when varying the R_{sh} , using a previously developed optoelectronic model¹⁶ with all other device parameters kept constant at the values used in ref 16. In addition, calculations predict a 15% relative improvement in the FF and thus in the overall device performance if R_{sh} can be increased to $1000 \Omega \text{ cm}^2$.¹⁴ Hence, a simple but reliable approach toward mitigation of shunt losses in early-stage thin-film devices may allow for rapid material and device evaluation before final device optimization is completed, with a reduced risk of “false negatives” from shunting.

In this work, we investigate the root cause of shunting losses in thin-film solar cells and its impact on performance and performance reproducibility. We study SnS thin-film substrate-style solar cells. We test the hypothesis that many of our solar cells suffer from a low device shunt resistance due to pinholes in the SnS absorber bulk. We use electron-beam-induced current (EBIC) measurements to image through-thickness

current pathways in the SnS absorber. We demonstrate a two-step absorber deposition approach that appears to block pinholes and thus improves the shunt resistance R_{sh} . As a result, we observe enhanced solar cell performance and performance reproducibility.

The design of a robust thin-film device architecture will be essential for our ongoing work on SnS bulk engineering and testing the impact on device performance. The two-step deposition method will allow the use of more conductive buffer layers in substrate-style device configurations. Here, we use tin sulfide as a proof-of-concept material system. Device shunting due to pinhole formation has been observed in other polycrystalline thin-film materials as well. Novel polycrystalline absorber materials such as antimony selenide (Sb_2Se_3)¹⁷ and copper antimony sulfide (CuSbS_2)¹⁸ have been successfully applied in photovoltaic devices. However, low shunt resistances have been reported which may limit the device performance to date. When exploring novel promising classes of materials for thin-film device applications (e.g., nitride semiconductors for solar energy conversion¹⁹), it will be important to avoid false-negatives due to device shunting. The here presented two-step absorber deposition approach (in particular the combination of a high-temperature and subsequent low-temperature step) is generalizable and may be applicable to a variety of novel thin-film materials (potentially even beyond photovoltaic applications).

2. EXPERIMENTAL METHODS

SnS substrate-style devices were fabricated on commercial Si/SiO₂ wafers. The wafers were cleaned in a hot solvent bath and nitrogen-dried prior to the molybdenum (Mo) back contact deposition. The SnS bulk was deposited in a single-source custom-made thermal evaporator at a substrate temperature of $(240 \pm 30) \text{ }^\circ\text{C}$. Further details on the back contact and absorber bulk deposition can be found in ref 14. The SnS bulk was annealed for 60 min in 4% H₂S in N₂ at $400 \text{ }^\circ\text{C}$, with a total pressure of $(28 \pm 1) \text{ Torr}$. For the SnS one-step deposition baseline devices, the thermally evaporated SnS thin-film was exposed to ambient air for 24 h to grow a thin SnO_x layer prior to the buffer layer deposition. For the two-step absorber deposition devices, the thermally evaporated SnS thin-film was transferred from the annealing furnace to the atomic layer deposition (ALD) chamber. During the transfer, the film was exposed to air for less than 2 min. A second thin SnS absorber layer (75 nm) was grown via ALD at $200 \text{ }^\circ\text{C}$ before applying the same surface oxidation procedure as to the baseline SnS samples. The *n*-type buffer layer was grown via ALD at $120 \text{ }^\circ\text{C}$ on all SnS device samples, comprising 30 nm of nitrogen-doped Zn(O,S) with a S/Zn ratio of 1:14 and 10 nm ZnO. Indium tin oxide (ITO) with a sheet resistance of $40 \Omega/\text{sq}$ was sputtered as the transparent top contact, using a shadow mask. Ag fingers and contact pads were deposited via e-beam evaporation and used for metallization.

The morphology of the SnS thin-films was imaged by field-emission scanning electron microscopy (FESEM, Zeiss, Ultra-55). Cross-sectional EBIC measurements were performed at MIT, using an FEI Helios NanoLab dual-beam system equipped with a Point Electronic DISS 5 EBIC system, at an accelerating voltage of 5 kV and beam current of 86 pA. The device cross section was polished before the EBIC measurement using argon ion milling (JEOL cross-sectional polisher), at an accelerating voltage of 5 kV and argon flow rate of 6 sccm for 4 h.

The solar cells were characterized at room temperature ($24.9 \text{ }^\circ\text{C}$) by current density–voltage (J – V) and external quantum efficiency (EQE) measurements at MIT, using a Keithley 2400 sourcemeter. The standard illumination of 100 mW cm^{-2} was generated by a Newport Oriel 91194 solar simulator with a 1300 W Xe-lamp using an AM1.5G filter, and a Newport Oriel 68951 flux controller calibrated by a silicon reference cell equipped with a BK-7 window, certified by the National

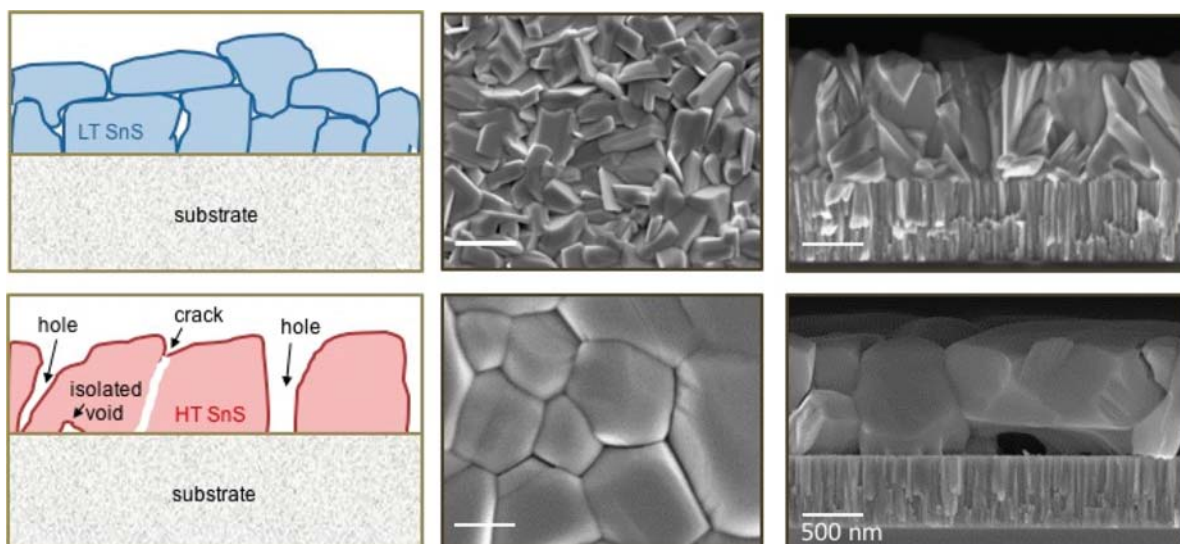


Figure 2. Morphology comparison of as-deposited SnS thin-films at 240 °C (top) and sister samples annealed at 400 °C in an H₂S atmosphere. (Left) Simplified schematics comparing dense packing of smaller grains (<500 nm) at low temperature (LT) and grain growth as well as void formation at high temperature (HT). (Right) Plane-view and cross-sectional SEM of SnS thin-film before and after H₂S annealing at 400 °C. The scale bar is 500 nm.

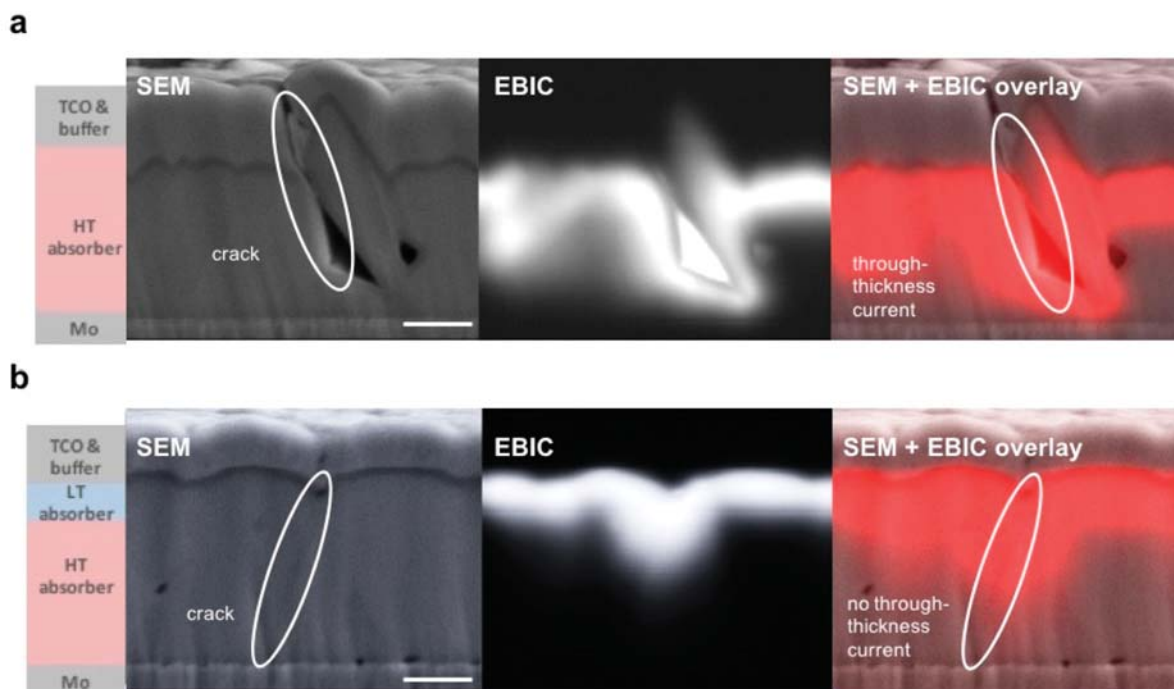


Figure 3. Cross-sectional SEM and EBIC measurements of SnS substrate-style devices. (a) One-step absorber deposition with high-temperature (HT) treatment as applied in the baseline SnS substrate-style device architecture. Cracks in the annealed SnS bulk become preferred through-thickness current pathways, creating pathways of lower resistance between the Mo back contact and the buffer layer and transparent conductive oxide (TCO) on top, as demonstrated in the EBIC image. (b) Two-step absorber deposition approach employing a second, thin SnS overlayer deposited via ALD at low temperature (LT) to fill voids in the HT SnS bulk and to prevent detrimental through-thickness current pathways. Despite the appearance of a crack in the absorber layer, there is no through-thickness EBIC signal that would indicate a shunt pathway. The scale bar is 400 nm.

Renewable Energy Laboratory (NREL). The area of each device is 0.27 cm², defined by the ITO area. The EQE measurements were performed with a PV Measurements Model QEX7 tool. In addition, a representative SnS baseline device was characterized with and without a light mask (area of 0.22 cm²) by the cell certification team at NREL. The light mask is used as an additional tool to define the active device area under illumination. Device simulations were performed using a

solar cell capacitance simulator (SCAPS).²⁰ The shunt resistance R_{sh} in the dark and under illumination was derived from the slope of the $J-V$ curve at zero voltage.

3. RESULTS AND DISCUSSION

3.1. High-Temperature Treatment of Polycrystalline Thin-Films. High-temperature (HT) treatments have been shown to stimulate grain growth in various polycrystalline thin-film absorber materials (e.g., CZTS,^{21–23} CdTe,²⁴ and lead halide perovskites²⁵), contributing to enhanced device performances due to reduced charge carrier recombination losses at grain boundaries. Similarly, we have found HT treatments of the SnS absorber films to result in significant grain growth and increased charge-carrier transport properties.^{26,27} Figure 2 reveals plane-view and cross-sectional scanning electron micrographs (SEM) comparing small-grained (<500 nm), as-deposited SnS thin-films at 240 °C (top row) to large-grained (~1 μm), annealed SnS thin-films at 400 °C in H₂S atmosphere (bottom row).

HT treatments, however, may also cause voids and cracks in the polycrystalline SnS thin-films due to locally unfavorable surface energetics and/or coefficients of thermal expansion. The SEM of the annealed SnS thin-films suggest some void formation along grain boundaries. The simplified schematics on the left illustrate the effect of HT treatment on the thin-film morphology. The as-deposited film at LT (here 240 °C) is densely packed, forming a continuous film. The annealed film at HT exhibits discontinuities due to the formation of holes, cracks, and/or isolated voids upon grain growth. Note that these discontinuities upon HT treatment have been observed in SnS thin-films independent of the deposition technique (thermal evaporation and atomic layer deposition).²⁸

When depositing the ALD *n*-type buffer material post absorber treatment, it may fill voids in the underlying HT absorber bulk, providing direct current pathways between the Mo back contact and the *n*-type buffer layer. ALD is known to provide conformal coating even in high-aspect-ratio gaps and trenches.²⁹ In the traditional device architectures as used in ref 14, the choice of buffer layer is thus limited to semi-insulating materials. To enable the use of more conductive buffer layer materials, which may promote beneficial interface band bending in the absorber layer, we develop a simple approach to fill voids in the HT SnS bulk. We propose the deposition of a thin, continuous SnS overlayer prior to the buffer deposition. We process the second, thin SnS overlayer (75 nm) via ALD and at a lower temperature (120 °C) to grow densely packed small SnS grains.

3.2. Two-Step Absorber Deposition Approach. We use cross-sectional SEM and EBIC to visualize the impact of the two-step deposition approach on pinhole-filling and device shunting. Results are compared to the one-step deposition baseline device. Figure 3 reveals device cross sections of a representative one-step deposition baseline device (Figure 3a) and a representative two-step deposition device (Figure 3b). The SEMs on the left reveal cracks in the annealed SnS bulk in both devices. For the baseline device, the EBIC data shows current collection along the entire length of the crack, implying that the crack in the baseline device becomes a through-thickness current pathway, reducing the shunt resistance of the device. In the two-step deposition device, however, the LT SnS overlayer appears to successfully coat the bottom of the crack in the HT SnS bulk, preventing a detrimental through-thickness current pathway. The EBIC data in Figure 3b suggests that the crack is only partially filled by the LT SnS. We detect no through-thickness current in EBIC at the location of the through-thickness crack in the two-step device.

Note that Figure 3 shows only a small area of each device, focusing on a representative crack between two large SnS grains. We compared the cross section of each representative device over a lateral distance of 500 μm. In total, we observe 10 cracks in the SnS absorber layer in the one-step deposition baseline device and 6 cracks in the two-step absorber deposition device, which may contribute to the device leakage current. In the one-step deposition device, we identify 5 out of the 10 cracks as performance-limiting through-thickness current pathways. In the two-step deposition device, however, we observe only 1 through-thickness current pathway out of 6 detectable cracks. Based on the present EBIC data, the likelihood of cracks resulting in through-thickness current pathways is reduced from 50% to 16%. Table 1 summarizes the numbers of cracks and through-thickness current pathways for both device types.

Table 1. Numbers of Cracks and Through-Thickness Current Pathways in the SnS Absorber Bulk That Are Observed in a Representative One-Step Deposition Device and Two-Step Deposition Device Across a Total Lateral Distance of 500 μm

device architecture	no. of detectable cracks (SEM)	no. of through-thickness current pathways (EBIC)
one-step deposition	10	5
two-step deposition	6	1

The EBIC data indicate a lower through-thickness crack density and lower through-thickness currents in the two-step absorber deposition devices. Because EBIC is a powerful but time-intensive measurement technique, the data presented here do not provide enough statistics to quantify fully the impact of the two-step deposition approach on device shunting, but rather they show a relative comparison within the studied device areas.

3.3. Tin Sulfide Solar Cells. Next, we performed current density–voltage (*J*–*V*) measurements on 11 identically processed SnS one-step deposition baseline devices and two-step deposition devices. The distribution of *J*–*V* curves measured in the dark and under 1 sun illumination is shown in Figure 4a,b. While both sample sets—baseline (red lines) and two-step deposition (blue lines)—contain one heavily shunted cell each, we observe a broader performance spread across the baseline cells. In Figure 4c, we compare the *J*–*V* curves of one representative one-step deposition baseline device (red lines) and one two-step deposition device (blue lines), indicating a high *V*_{OC} of 370 mV and a low leakage current density of 18 nA/cm² in short-circuit condition for the two-step deposition device. The solar cell characteristics of the two representative devices from Figure 4c are listed in Table 2. Both devices were measured under similar conditions without a light mask at MIT. We observe a 5.6% relative improvement in the *V*_{OC} and 5.1% relative improvement in the FF for the two-step deposition device compared to the one-step deposition baseline device due to improvements in the shunt resistance *R*_{sh} by more than a factor of 3.5 under illumination and a factor of 30 in the dark. The *J*_{SC} of the two-step deposition device, however, is 3.7% lower relative to the one-step deposition device. The overall device efficiency reveals a slight improvement by 7% relative from 3.80% to 4.08% experimentally (see Table 2).

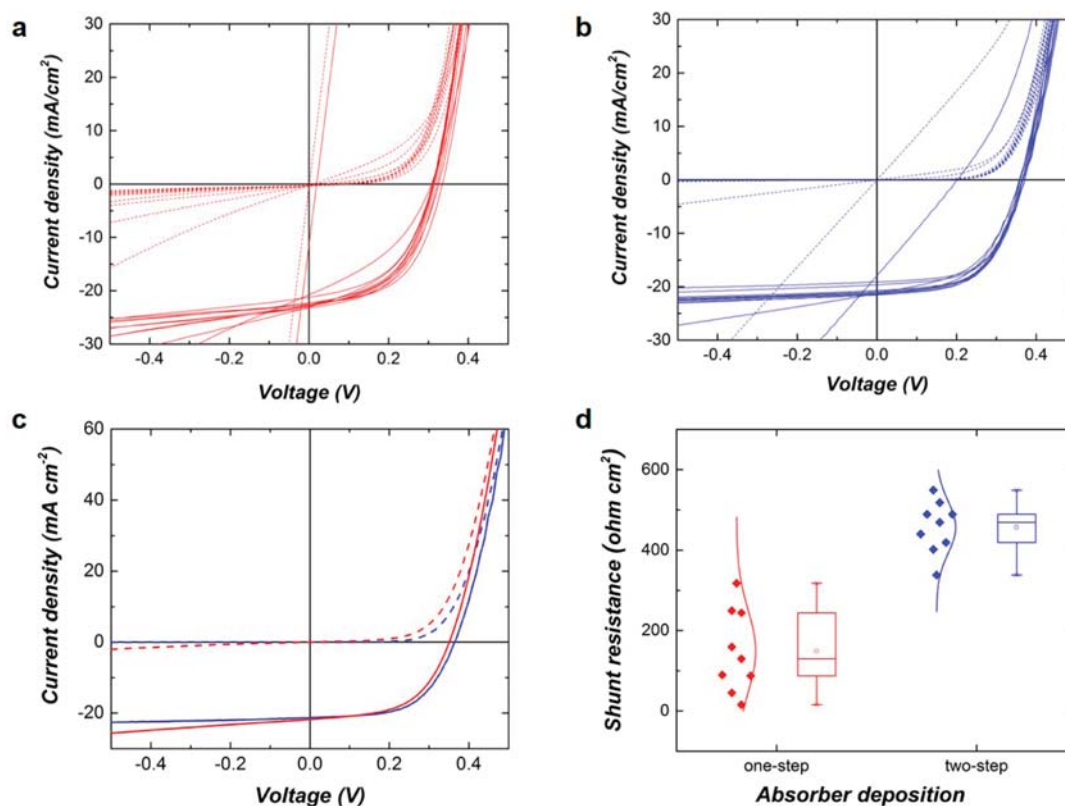


Figure 4. Comparison of SnS solar cell data of the baseline device which includes a high-temperature (HT) absorber treatment and the two-step absorber deposition device which uses a low-temperature (LT) absorber overlayer on top of the HT treated absorber bulk. (a,b) Distribution of J - V characteristics in the dark (dashed lines) and under 1 sun illumination (solid lines) for 11 identically processed devices following the baseline processing protocol (plot (a), red lines) and the two-step absorber deposition (plot (b), blue lines), respectively. (c) Directly compares the J - V data of two representative devices (baseline HT and two-step deposition HT+LT). (d) Compares the illuminated shunt resistance R_{sh} of the baseline HT and two-step deposition HT + LT SnS devices, excluding heavily shunted devices.

Table 2. Solar Cell Device Data for the Representative One-Step Deposition Baseline and Two-Step Deposition Device Characterized at MIT and at NREL, with and without Light Mask

device	facility	light mask	V_{OC} [mV]	J_{SC} [mA/cm ²]	% FF	% PCE
one-step dep.	MIT	no	350.8	19.9	54.3	3.80
two-step dep.	MIT	no	370.6	19.2	57.1	4.08
one-step dep.	NREL	no	351.9	20.0	53.5	3.78
one-step dep.	NREL	yes	342.5	19.5	55.0	3.69

An independent J - V measurement on the representative baseline device was performed at NREL with and without light mask, indicating a 2–3% relative decrease in V_{OC} and J_{SC} and a 2–3% increase in the FF, when applying the light mask. Comparing the measurements at MIT and at NREL suggests that the J_{SC} measurements at MIT yield an 8.5% overestimate. The V_{OC} and FF measurements at MIT and NREL without light mask are within the statistical error.

The shunt resistance R_{sh} was computed from the dark and illuminated J - V data in reverse bias for nine identically processed baseline and two-step deposition devices. We compare the light R_{sh} for the HT baseline and the HT+LT two-step deposition device in Figure 4d. We exclude two

baseline and two-step deposition devices due to heavy shunting because we attribute the shunting in these cases to macroscopic shunts formed during sample handling. The median light R_{sh} improved from 129 Ω cm² for the one-step baseline devices to 469 Ω cm² for the HT+LT two-step deposition devices (>factor of 3.5). The median dark R_{sh} improved from 134 Ω cm² to 3997 Ω cm² (factor of 30).

For the HT+LT device, we observe a R_{sh} reduction (factor of 8.5) upon illumination, which hints at some voltage-dependent collection efficiency. Note that the HT SnS bulk and the LT SnS overlayer are processed via different deposition techniques (thermal evaporation and atomic layer deposition) as well as at different temperatures. This may affect charge collection at the SnS absorber/buffer interface. Overall, the narrower distribution of the light R_{sh} indicates an improved performance reproducibility for the HT+LT devices with standard errors $\sigma_{R_{sh}}$ of 21 Ω cm² compared to 34 Ω cm² for the baseline devices.

4. SUMMARY AND CONCLUSIONS

In this work, we have developed a simple approach to mitigate shunt losses in thin-film solar cells that may result from pinhole formation in polycrystalline materials. By engineering a two-step absorber deposition method, we demonstrate a robust substrate-style device architecture, which appears to successfully eliminate through-thickness current pathways in the polycrystalline absorber bulk.

We test this approach on tin sulfide (SnS) thin-film solar cells as a proof-of-concept. The two-step deposition yields a more than 3.5 \times superior device shunt resistance under illumination compared to the more standard approach of using a semi-insulating buffer layer directly on top of the annealed absorber bulk. Improvements in the shunt resistance are correlated to gains in the open-circuit voltage and fill factor, resulting in an overall device performance improvement from 4.15% to 4.44% (both devices measured at MIT). Even more importantly, the newly engineered devices, incorporating the two-step absorber deposition, reveal higher performance reproducibility.

It is worth noting that the baseline devices used in this study were initially fabricated and characterized at MIT in February 2014. The here presented data in Figure 4c and Table 2, however, were taken in March 2016 at MIT and NREL. Comparing the data sets from 2014 (see ref 14) and 2016, we do not observe any evidence of materials degradation despite ambient air exposure for 24 months.

AUTHOR INFORMATION

Corresponding Authors

*E-mail: vsteinma@mit.edu.

*E-mail: buonassisi@mit.edu.

Notes

The authors declare no competing financial interest.

ACKNOWLEDGMENTS

The authors thank K. Emery from the cell certification team at the National Renewable Energy Laboratory for his assistance with current density–voltage measurements, M. L. Castillo for her help with substrate preparation, and J. R. Poindexter and R.L.Z. Hoye for fruitful scientific discussions. This work was supported by a TOTAL SA grant, by the Engineering Research Center Program of the National Science Foundation, by the Office of Energy Efficiency and Renewable Energy of the Department of Energy under NSF Cooperative Agreement No. EEC-1041895, and by the U.S. Department of Energy through the SunShot Initiative under contract DE-EE0005329. V.S., R.C., R.E.B., and A.P. acknowledge the support of the Alexander von Humboldt foundation, a MITEI/TOTAL Energy fellowship, and two NSF GRFP fellowships, respectively. This work made use of the Center for Materials Science and Engineering at MIT which is supported by the NSF under award DMR-08-19762, and the Center for Nanoscale Systems at Harvard University which is supported by NSF under award ECS-0335765.

REFERENCES

- (1) Brandt, R. E.; Stevanović, V.; Ginley, D. S.; Buonassisi, T. Identifying Defect-Tolerant Semiconductors with High Minority-Carrier Lifetimes: Beyond Hybrid Lead Halide Perovskites. *MRS Commun.* **2015**, *5* (02), 265–275.
- (2) Walsh, A. Principles of Chemical Bonding and Band Gap Engineering in Hybrid Organic-Inorganic Halide Perovskites. *J. Phys. Chem. C* **2015**, *119*, 5755.
- (3) Zakutayev, A.; Caskey, C. M.; Fioretti, A. N.; Ginley, D. S.; Vidal, J.; Stevanovic, V.; Tea, E.; Lany, S. Defect Tolerant Semiconductors for Solar Energy Conversion. *J. Phys. Chem. Lett.* **2014**, *5* (7), 1117–1125.
- (4) Hao, F.; Stoumpos, C. C.; Cao, D. H.; Chang, R. P. H.; Kanatzidis, M. G. Lead-Free Solid-State Organic-Inorganic Halide Perovskite Solar Cells. *Nat. Photonics* **2014**, *8* (6), 489–494.

- (5) Noel, N. K.; Stranks, S. D.; Abate, A.; Wehrenfennig, C.; Guarnera, S.; Haghighirad, A.-A.; Sadhanala, A.; Eperon, G. E.; Pathak, S. K.; Johnston, M. B.; Petrozza, A.; Herz, L. M.; Snaith, H. J. Lead-Free Organic-Inorganic Tin Halide Perovskites for Photovoltaic Applications. *Energy Environ. Sci.* **2014**, *7*, 3061–3068.
- (6) Kumar, M. H.; Dharani, S.; Leong, W. L.; Boix, P. P.; Prabhakar, R. R.; Baikie, T.; Shi, C.; Ding, H.; Ramesh, R.; Asta, M.; Graetzel, M.; Mhaisalkar, S. G.; Mathews, N. Lead-Free Halide Perovskite Solar Cells with High Photocurrents Realized through Vacancy Modulation. *Adv. Mater.* **2014**, *26* (41), 7122–7127.
- (7) Yokoyama, T.; Cao, D. H.; Stoumpos, C. C.; Song, T.-B.; Sato, Y.; Aramaki, S.; Kanatzidis, M. G. Overcoming Short-Circuit in Lead-Free CH₃NH₃SnI₃ Perovskite Solar Cells via Kinetically Controlled Gas Solid Reaction Film Fabrication Process. *J. Phys. Chem. Lett.* **2016**, *7* (5), 776–782.
- (8) Swartz, G. A. Electrolytic Etch for Eliminating Shorts and Shunts in Large Area Amorphous Silicon Solar Cells. Patent US4385971A, May 31, 1983.
- (9) Tessema, M. M.; Giolando, D. M. Pinhole Treatment of a CdTe Photovoltaic Device by Electrochemical Polymerization Technique. *Sol. Energy Mater. Sol. Cells* **2012**, *107*, 9–12.
- (10) Ramakrishna Reddy, K. T.; Koteswara Reddy, N.; Miles, R. W. Photovoltaic Properties of SnS Based Solar Cells. *Sol. Energy Mater. Sol. Cells* **2006**, *90* (18–19), 3041–3046.
- (11) Sinsermsuksakul, P.; Heo, J.; Noh, W.; Hock, A. S.; Gordon, R. G. Atomic Layer Deposition of Tin Monosulfide Thin-Films. *Adv. Energy Mater.* **2011**, *1* (6), 1116–1125.
- (12) Hartman, K.; Johnson, J. L.; Bertoni, M. I.; Recht, D.; Aziz, M. J.; Scarpulla, M. a.; Buonassisi, T. SnS Thin-Films by RF Sputtering at Room Temperature. *Thin Solid Films* **2011**, *519* (21), 7421–7424.
- (13) Siebentritt, S. What Limits the Efficiency of Chalcopyrite Solar Cells? *Sol. Energy Mater. Sol. Cells* **2011**, *95* (6), 1471–1476.
- (14) Steinmann, V.; Jaramillo, R.; Hartman, K.; Chakraborty, R.; Brandt, R. E.; Poindexter, J. R.; Lee, Y. S.; Sun, L.; Polizzotti, A.; Park, H. H.; Gordon, R. G.; Buonassisi, T. 3.88% Efficient Tin Sulfide Solar Cells Using Congruent Thermal Evaporation. *Adv. Mater.* **2014**, *26* (44), 7488–7492.
- (15) Sinsermsuksakul, P.; Sun, L.; Lee, S. W.; Park, H. H.; Kim, S. B.; Yang, C.; Gordon, R. G. Overcoming Efficiency Limitations of SnS-Based Solar Cells. *Adv. Energy Mater.* **2014**, *4* (15), 1400496.
- (16) Mangan, N. M.; Brandt, R. E.; Steinmann, V.; Jaramillo, R.; Yang, C.; Poindexter, J. R.; Chakraborty, R.; Park, H. H.; Zhao, X.; Gordon, R. G.; Buonassisi, T. Framework to Predict Optimal Buffer Layer Pairing for Thin-Film Solar Cell Absorbers: A Case Study for Tin Sulfide/zinc Oxysulfide. *J. Appl. Phys.* **2015**, *118* (11), 115102.
- (17) Zhou, Y.; Wang, L.; Chen, S.; Qin, S.; Liu, X.; Chen, J.; Xue, D.-J.; Luo, M.; Cao, Y.; Cheng, Y.; Sargent, E. H.; Tang, J. Thin-Film Sb₂Se₃ Photovoltaics with Oriented One-Dimensional Ribbons and Benign Grain Boundaries. *Nat. Photonics* **2015**, *9* (6), 409–415.
- (18) Welch, A. W.; Baranowski, L. L.; Zawadzki, P.; DeHart, C.; Johnston, S.; Lany, S.; Wolden, C. A.; Zakutayev, A. Accelerated Development of CuSbS₂ Thin-Film Photovoltaic Device Prototypes. *Prog. Photovoltaics* **2016**, *24*, 929–939.
- (19) Zakutayev, A. Design of Nitride Semiconductors for Solar Energy Conversion. *J. Mater. Chem. A* **2016**, *4* (c), 6742–6754.
- (20) Burgelman, M.; Verschraegen, J.; Degraeve, S.; Nollet, P. Modeling Thin-Film PV Devices. *Prog. Photovoltaics* **2004**, *12* (23), 143–153.
- (21) Katagiri, H.; Jimbo, K.; Maw, W. S.; Oishi, K.; Yamazaki, M.; Araki, H.; Takeuchi, A. Development of CZTS-Based Thin-Film Solar Cells. *Thin Solid Films* **2009**, *517* (7), 2455–2460.
- (22) Hlaing Oo, W. M.; Johnson, J. L.; Bhatia, A.; Lund, E. A.; Nowell, M. M.; Scarpulla, M. A. Grain Size and Texture of Cu₂ZnSnS₄ Thin-Films Synthesized by Cosputtering Binary Sulfides and Annealing: Effects of Processing Conditions and Sodium. *J. Electron. Mater.* **2011**, *40* (11), 2214–2221.
- (23) Gershon, T.; Shin, B.; Bojarczuk, N.; Hopstaken, M.; Mitzi, D. B.; Guha, S. The Role of Sodium as a Surfactant and Suppressor of

Non-Radiative Recombination at Internal Surfaces in Cu₂ZnSnS₄. *Adv. Energy Mater.* **2015**, *5* (2), 1400849.

(24) Romeo, A.; Bätzner, D. L.; Zogg, H.; Tiwari, A. N. Recrystallization in CdTe/CdS. *Thin Solid Films* **2000**, *361*-362, 420-425.

(25) Xiao, Z.; Dong, Q.; Bi, C.; Shao, Y.; Yuan, Y.; Huang, J. Solvent Annealing of Perovskite-Induced Crystal Growth for Photovoltaic-Device Efficiency Enhancement. *Adv. Mater.* **2014**, *26* (37), 6503-6509.

(26) Chakraborty, R.; Steinmann, V.; Mangan, N. M.; Brandt, R. E.; Poindexter, J. R.; Jaramillo, R.; Mailoa, J. P.; Hartman, K.; Polizzotti, A.; Yang, C.; Gordon, R. G.; Buonassisi, T. Non-Monotonic Effect of Growth Temperature on Carrier Collection in SnS Solar Cells. *Appl. Phys. Lett.* **2015**, *106*, 203901.

(27) Jaramillo, R.; Sher, M.-J.; Ofori-Okai, B. K.; Steinmann, V.; Yang, C.; Hartman, K.; Nelson, K. A.; Lindenberg, A. M.; Gordon, R. G.; Buonassisi, T. Transient Terahertz Photoconductivity Measurements of Minority-Carrier Lifetime in Tin Sulfide Thin-Films: Advanced Metrology for an Early Stage Photovoltaic Material. *J. Appl. Phys.* **2016**, *119* (3), 035101.

(28) Park, H. H.; Heasley, R.; Sun, L.; Steinmann, V.; Jaramillo, R.; Hartman, K.; Chakraborty, R.; Sinsermsuksakul, P.; Chua, D.; Buonassisi, T.; Gordon, R. G. Co-Optimization of SnS Absorber and Zn(O,S) Buffer Materials for Improved Solar Cells. *Prog. Photovoltaics* **2015**, *23* (7), 901-908.

(29) Gordon, R. G.; Hausmann, D.; Kim, E.; Shepard, J. A Kinetic Model for Step Coverage by Atomic Layer Deposition in Narrow Holes or Trenches. *Chem. Vap. Deposition* **2003**, *9* (2), 73-78.